9-20-2018

Morphology and stress evolution during the initial stages of intergranular corrosion of X70 steel

Denizhan Yavas
Iowa State University, dyavas@iastate.edu

Abdullah Alshehri
Iowa State University

Pratyush Mishra
Iowa State University, mishra@iastate.edu

Pranav Shrotriya
Iowa State University, shrotriy@iastate.edu

Ashraf F. Bastawros
Iowa State University, bastaw@iastate.edu

See next page for additional authors

Morphology and stress evolution during the initial stages of intergranular corrosion of X70 steel

Abstract

Pipeline steels are vulnerable to stress corrosion cracking (SCC) during intergranular corrosion (IGC) at potentials of active dissolution in moderately alkaline carbonate-bicarbonate solutions. Morphology evolution accompanying IGC has not been fully described, despite the relevance of the corrosion geometry to crack initiation. The present article reports a characterization of concurrent morphology and mechanical stress development during the initial stages of IGC of X70 steel in sodium bicarbonate solution, in the potential range of high SCC susceptibility. Morphology was revealed by scanning electron microscope examination of cross sections through the IGC layer, and stress evolution was monitored by curvature interferometry. At potentials in the range of SCC susceptibility, IGC creates triangular wedges of porous corrosion product centered at grain boundary triple junctions. The wedge shape indicates a higher corrosion rate at the grain boundary compared to the grain surfaces. Compressive stress is generated during IGC due to internal oxidation on grain surfaces forming a thin compact corrosion product layer. Polarization at a potential below the SCC range resulted in selective grain dissolution with no internal corrosion product or compressive stress increase. Silicon solute atoms are selectively oxidized into the compact grain boundary corrosion product film.

Keywords

High-strength steel alloys, Intergranular corrosion, Stress corrosion cracking, Pipeline steel

Disciplines

Aerospace Engineering | Chemical Engineering | Mechanical Engineering | Metallurgy | Structures and Materials

Comments

This is a manuscript of an article published as Yavas, Denizhan, Abdullah Alshehri, Pratyush Mishra, Pranav Shrotriya, Ashraf F. Bastawros, and Kurt R. Hebert. "Morphology and stress evolution during the initial stages of intergranular corrosion of X70 steel." *Electrochimica Acta* 285 (2018): 336-343. DOI: 10.1016/j.electacta.2018.07.207. Posted with permission.

Authors

Denizhan Yavas, Abdullah Alshehri, Pratyush Mishra, Pranav Shrotriya, Ashraf F. Bastawros, and Kurt R. Hebert

Morphology and Stress Evolution During the Initial Stages of Intergranular Corrosion of X70 Steel

Denizhan Yavas[a,], Abdullah Alshehri[b], Pratyush Mishra[c], Pranav Shrotriya[b], Ashraf F. Bastawros[a], and Kurt R. Hebert[c,*]

[a]Department of Aerospace Engineering, Iowa State University, Ames, IA, 50011, United States

[b]Department of Mechanical Engineering, Iowa State University, Ames, IA, 50011, United States

[c]Department of Chemical and Biological Engineering, Iowa State University, Ames, IA, 50011, United States

* Corresponding author: E-mail: krhebert@iastate.edu

Keywords: high-strength steel alloys, intergranular corrosion, stress corrosion cracking, pipeline steel

Abstract

Pipeline steels are vulnerable to stress corrosion cracking (SCC) during intergranular corrosion (IGC) at potentials of active dissolution in moderately alkaline carbonate-bicarbonate solutions. Morphology evolution accompanying IGC has not been fully described, despite the relevance of the corrosion geometry to crack initiation. The present article reports a characterization of concurrent morphology and mechanical stress development during the initial stages of IGC of X70 steel in sodium bicarbonate solution, in the potential range of high SCC susceptibility. Morphology was revealed by scanning electron microscope examination of cross sections through the IGC layer, and stress evolution was monitored by curvature interferometry. At potentials in the range of SCC susceptibility, IGC creates triangular wedges of porous corrosion product centered at grain boundary triple junctions. The wedge shape indicates a higher corrosion rate at the grain boundary compared to the grain surfaces. Compressive stress is generated during IGC due to internal oxidation on grain surfaces forming a thin compact corrosion product layer. Polarization at a potential below the SCC range resulted in selective grain dissolution with no internal corrosion product or compressive stress increase. Silicon solute atoms are selectively oxidized into the compact grain boundary corrosion product film.

1. Introduction

Pipeline steels are susceptible to both intergranular stress corrosion cracking (SCC) and intergranular corrosion (IGC) in “high-pH" (i. e. pH 8-10) carbonate-bicarbonate solutions [1, 2]. IGC and SCC occur at the same pH values, and in the same well-defined range of potentials within the active dissolution peak of the steel polarization curve [3-7]. The equivalent conditions for SCC and IGC suggest that the corrosion process itself is directly responsible for grain boundary embrittlement. Mechanisms proposed for corrosion-induced embrittlement have included formation of geometric features such as notches that concentrate external stress, or creation of brittle surface layers or films on corroding surfaces [8]. Much of the prior research on intergranular corrosion of pipeline steels has concerned the nature of electrochemical corrosion reactions and products within the critical potential range [9-15]. It is found that dissolution near the potential of the active dissolution current peak produces Fe(II) hydroxide and carbonate species, while at potentials above the active region insoluble Fe(III) products are found. Also, the potential ranges of both IGC and intergranular SCC has been shown to lie between the active peak and the passivation potential, in which both Fe(II) and Fe(III) products are formed. However, this work did not establish a relationship between the electrochemistry of corrosion within the critical potential range and the SCC mechanism. Also, no prior work to our knowledge focused on the role of grain boundaries in the corrosion process, which is clearly central to an understanding of intergranular SCC.

Because of the close coupling between intergranular corrosion and stress corrosion cracking of pipeline steels, it is important to identify aspects of corrosion at grain boundaries that are relevant to the evolving mechanical properties of the near-surface region. Corrosion

morphology development is potentially significant because the geometry of the corroded region determines its response to external tensile stress. Further, intergranular corrosion rates can be inferred by observing grain boundary morphology evolution. Despite the relevance of intergranular corrosion to high-pH SCC of pipeline steels, no detailed characterization of grain boundary morphology evolution during IGC of ferritic steels has been reported in the literature, in contrast to the knowledge base about such processes on austenitic stainless steels [16]. Also, it has been proposed that corrosion-induced wedging stress at grain boundaries can assist crack initiation and growth [17-20]. However, very few studies exist on stress evolution accompanying corrosion along grain boundaries. Recently, we reported a nanoindentation study of corroded X70 pipeline steel which suggested that corrosion directly induces mechanical property changes at grain boundaries [21, 22]. The experiments revealed 1 μm-thick mechanically degraded layers adjacent to corroded grain boundaries with 25% lower hardness relative to the grain interior. Further knowledge of corrosion reactions at grain boundaries is needed to understand the origin of grain boundary softening and its relation to SCC.

The present study focuses on morphology and mechanical stress evolution during high-pH intergranular corrosion of X70 pipeline steel in sodium bicarbonate solution. Scanning electron microscope (SEM) examination of cross sections through the IGC-affected subsurface layer were used to characterize the spatial distribution of metal dissolution and corrosion product formation in relation to the grain microstructure, at potentials within the range of highest SCC susceptibility. It is found that within the critical potential range, IGC produces triangular wedges of corrosion product around grain boundary triple junctions. The wedge shape is due to local enhancement of the corrosion rate on the grain boundary itself relative to the grain surfaces.

Mechanical stress evolution during corrosion was monitored using in situ stress measurements and related to internal oxidation within the IGC layer.

2. Experimental details

Samples of a high strength low-alloy pipeline steel (API X70) were machined from a pipe wall. The specimens of 1 mm thickness were cut along the long axis of the pipe, with the top surface in the longitudinal-short transverse plane. The sample length and width dimensions were 18 mm x 18 mm for . The main alloying elements in X70 were Mn (~1.75 wt. %), Si (~0.45 wt. %), and C (~ 0.17 wt. %). The minority pearlite phase was composed of grains less than 5 μm in width and elongated in the longitudinal direction, while the majority ferrite phase was made up of nearly equiaxed grains of typically 5 μm size. The sample surfaces were polished with 400, 600 and 800-grit sandpaper, followed by cleaning with deionized water and ethanol. Electrochemical experiments were carried out in a three-electrode cell with Pt wire counter electrode and Ag/AgCl reference electrode. All cited potentials are with respect to this reference. The test solution was naturally aerated aqueous 1 M $NaHCO_3$ at room temperature. Solutions were prepared using analytical grade reagents and deionized water (resistivity 18 MΩ-cm). The applied potential was first held at -1.0 V for 5 min to cathodically reduce surface oxide, and then stepped or scanned in the anodic direction.

For examination of the corrosion morphology in cross section, samples were polished to reveal planes at orientations either perpendicular to or at a shallow angle from the surface. Corrosion specimens were examined by scanning electron microscopy (SEM, FEI Quanta 250), and by non-contact optical profilometry (Zygo NewView 6200). In addition, focused ion beam (FIB) microscopy was utilized to reveal the corrosion morphology, using an ion beam at 52^o angle from the sample surface (FEI NanoLab Helios Dual Beam). A 1 μm thick and 15 μm long protective carbon strip was first deposited on the sample surface in order to preserve the top

corrosion product layer. Then, a trench with an area of 25 x 25 μm was ion-milled with a depth of about 5 μm. Finally, a finer ion-milling step with a reduced material removal rate was performed normal to the top surface to reveal the corrosion cross-section.

In situ stress measurements employed the phase shifting curvature interferometry method [23]. The applications of this technique to measure stress changes during corrosion and anodic oxidation of aluminum were described in earlier publications [20, 24]. One side of the steel sample was polished to a 0.05 μm particle finish using a diamond particle suspension and served as a reflective surface for interferometry. The specimen was mounted in a test cell with the unpolished side in contact with the electrolyte solution and the opposite side facing the optical system. Changes in sample curvature during corrosion were monitored. The curvature change ($d\kappa$) is related to the near-surface force per width (dF_w) according to the Stoney thin-film approximation,

$$dF_w = \frac{Y_s h_s^2}{6(1-\nu_s)} d\kappa \quad (1)$$

where Y_S, ν_S and h_S and are respectively the elastic modulus, Poisson's ratio and thickness of the steel sample. The force per width is the in-plane biaxial stress σ_{xx} integrated through the sample thickness,

$$F_w = \int_0^{h_s} \sigma_{xx} dz \quad (2)$$

where the *x* axis is parallel to the steel surface, and the z axis extends toward the bulk metal from its origin at the surface. Force per width is referenced to the initial state of the sample at the

beginning of anodic polarization. Compressive and tensile force changes are respectively negative and positive in sign.

3. Results and discussion

3.1. Electrochemical measurements

Fig. 1 (a) shows the active dissolution region of the polarization curve of X70 steel in 1 M $NaHCO_3$ solution. The potential region of susceptibility to IGC and SCC extends from the potential of the current peak at -0.6 V to the passivation potential at -0.4 V [4, 6, 7]. Three test potentials within this range were selected for potentiostatic experiments, as indicated in the Figure: -0.575 V, -0.521 V and -0.478 V. Examples of current transients at these potentials are shown in Fig. 1 (b). Initially, the current density decayed to a minimum value at 1 - 6 min at all three potentials. From rotating ring-disk electrode (RRDE) experiments Riley and Sykes found that the main reaction during the current decay is formation of a surface film [13]. Based on the charge density of 10 to 30 mC/cm^2 passed during the decay, the equivalent $Fe(OH)_2$ thickness is 14 - 40 nm, comparable to the thickness of 80 nm from XPS for the steady-state surface film at the peak potential [14]. At the two higher potentials, the current increased to a maximum after the initial decay and then slowly fell. No maximum was reached after 45 min at -0.575 V.

3.2. Large-angle cross-section samples

Large-angle cross section views of the steel interface after corrosion tests at -0.521 V for 2 and 4 hr are exhibited in Fig. 2 (a) and 2 (b) respectively. The 2 hr-exposed sample was prepared by FIB milling and the 4 hr sample by cross-sectioning and mechanical polishing. Both images in Fig. 2 illustrate the corrosion product film that covered the steel surface after the

current density maximum. The corrosion product films are the dark gray-shaded layers on the upper surfaces of the steel. In Fig. 2 (a), a 1 μm thick layer of carbon was deposited on the corrosion product to preserve it during ion milling. The white-shaded layer below the corrosion product is the finely ion-milled near-surface portion of the steel sample. The darker uneven area below the near-surface layer is the initially milled trench prior to fine cross-section ion-milling.

At both 2 hr and 4 hr, the corrosion product consists of particles several μm in width separated by small gaps. The void in the central part of the film in Fig. 2 (a) is atypical and may be caused by attrition of a corrosion product particle during sample preparation. EDS of the corrosion product layer in Fig. 2 (b) revealed that it contained Fe, O and C, suggesting that the film is an iron hydroxy-carbonate as found previously [10, 14, 15]. The Na/Fe concentration ratio of 0.15 found by EDS indicated that the product contained significant amount of sodium, consistent with the finding of sodium or potassium in the corrosion product in earlier studies [10, 15]. Incorporation of electrolyte Na^+ ions is evidence that the product is formed by precipitation. Nanoindentation measurements revealed an elastic modulus of 28 GPa for the product layer, much smaller than the value of about 200 GPa for dense iron oxide [22, 25]. The low modulus of the film suggests high porosity, also consistent with a precipitated film.

The precipitated corrosion product layer thickness measured from the cross-section images increased from 2.5 μm at 2 hr to 4.3 μm at 4 hr. The corresponding ratios of thickness to charge density were 1.9×10^{-4} cm^3/C at 2 hr and 1.6×10^{-4} cm^3/C at 4 hr. These values can be compared to the ratios associated with possible product layer constituents. The corrosion product formed in bicarbonate solutions is an iron hydroxycarbonate [15], which at -0.521 V may contain both and Fe(II) and Fe(III) compounds [9, 10, 13, 14]. The thickness-charge density ratio for compact product layers based on the molar volumes of $Fe(OH)_2$, $FeCO_3$ and $Fe(OH)_3$ are

respectively 1.4 x 10^{-4} , 1.5 x 10^{-4} and 9.5 x 10^{-5} cm^3/C. The porosity of the product layer is consistent with the somewhat larger ratios found experimentally.

The images in Fig. 2 (a) and (b) reveal a number of triangular wedges along the metal-corrosion product interface, marked by dashed lines. The wedges are positioned close to the gaps between corrosion product particles. These features were especially evident during FIB examination for Fig. 2 (a), as numerous wedge features located at different points on the surface appeared and disappeared as the sample cross section was ion-milled. The wedge angle is defined as shown in Fig. 2 as the angle at the apex of the triangular groove. Based on about 8 measurements at each exposure time, the wedge angle was 136 $\pm$ 6.4^o at 2 hr and 117 $\pm$ 17^o at 4 hr. The wedge depths are about 0.6 μm at 2 hr and 1 to 1.5 μm at 4 hr. Triangular wedges can be produced by intergranular attack, as discussed in the next section.

Fig. 3 exhibits a non-contact optical topological scan for an experiment in which the sample was exposed for 2 hr at -0.521 V. After the experiment, the corrosion product was removed by wiping the surface with a swab dipped in acetic acid. The profile spans parts of the rough corroded surface as well as surrounding surface (abscissa values smaller than 10 μm) that was not exposed to solution. The corroded area reveals minima with depths from 0.3 to 0.7 μm below the uncorroded area, and peaks that rise above the surrounding surface. The minima are apparently the triangular wedges marked by dashed lines in Fig. 2 (a), as both features have the same range of depths and similar lateral spacing. The peaks are likely remnants of corrosion product particles. If these particles are disregarded, the top surface heights inside and outside the corroded area are the same. It can therefore be concluded that there was no significant general corrosion on the surface

between the triangular wedges. A similar profile measured after 4 hr (not shown) also supports the absence of general corrosion. Thus, despite the overall appearance of the product layer as a uniform film, the corrosion process seems to exclusively consist of localized attack centered at shallow triangular wedges.

3.3. Small-angle cross section samples

Small-angle cross sections were prepared by polishing to reveal the internal corrosion morphology on planes nearly parallel to the external surface. Figure 4 exhibits SEM images of a steel specimen after a 2 hr corrosion exposure at -0.521 V. The current density transient for the same experiment is found in Fig. 1 (b). In the low magnification image in Fig. 4 (a), the intergranular corrosion layer lies between the precipitated corrosion product and uncorroded base alloy. The layer labeled corrosion product in Fig. 4 (a) is the same as the precipitated iron hydroxide-carbonate layer noted in Fig. 2. Note that distances along the vertical direction in these images magnify depth through the polishing angle. The magnification factor in this direction is approximately 1000, since the apparent thickness of the IGC layer in Fig. 4 (a) is 900 μm, while the FIB cross section (Fig. 2 (a)) reveals the true IGC layer thickness to be 0.9 μm. Figs. 4 (b) - (e) are higher-magnification views at selected depths within the IGC layer. Figs. 4 (d) and (e) illustrate that localized corrosion attack centers at grain boundary triple junctions between the equiaxed and approximately 5 μm diameter steel grains. Black-shaded crevices formed by corrosion at triple junctions are surrounded by roughly 1 μm thick gray-shaded corrosion product layers coating the white-shaded steel grains. In addition to progressing along the triple junctions, corrosion also penetrates laterally along the grain boundaries adjacent to the

triple junctions (Fig 4 (d)). At the interface between the metal and the top corrosion product layer (Fig. 4 (c)), the grain boundary product film surrounds isolated clusters of grains. The cores of these grain clusters are eventually converted to corrosion product, forming the particles comprising the film. Thus, the corrosion product morphology reflects that of the underlying grain structure.

The crevices along triple junctions in Fig. 4 correspond to the fissures at the triangular wedges in Fig. 2. Therefore, Figs. 4 (c) - (e) represent respectively the top, midpoint and apex of the triangular wedges in Fig. 2. Note that triple junction crevices are present in Fig. 2 only when the cross section plane lies close to the wedge apex. Since the triangular wedges are centered at triple junctions, they are indeed associated with intergranular attack. Triangular wedges have been observed during intergranular corrosion of austenitic stainless steels at transpassive potentials, and are considered to be characteristic features of "unsensitized" IGC in the absence of grain boundary precipitates [16, 26]. The wedge angle α is related to the ratio of the dissolution velocity of the grain boundary at the wedge apex (V_{gb}) to the wedge surface dissolution velocity (V_s),

$$\frac{V_{gb}}{V_s} = \frac{1}{sin(\alpha/2)} \tag{3}$$

The wedge angles in the present work suggest V_{gb}/V_s of 1.1 - 1.2, much smaller than the ratio of approximately 10 indicated by the relatively acute wedge angles in stainless steel [16]. To our knowledge, the triangular wedge morphology of IGC in pipeline steel has not been previously noted. However, Wendler-Kalsch found that corrosion in the potential range of SCC susceptibility produced 2 μm-deep grain boundary grooves similar in appearance to the wedges

in Fig. 2 [5]. No such grooves were observed in Ref. [5] at potentials higher than the upper limit of the SCC potential range, suggesting that the fundamental processes that produce the grain boundary wedge shape may intrinsically important in the SCC mechanism.

The important features of the intergranular corrosion geometry are depicted schematically in Fig. 5, which shows the triangular wedge morphology at the corroded triple junction. The wedge angle α and the corrosion velocities V_s and V_{gb} are defined in the figure. Fig. 5 also illustrates the precipitated porous corrosion product layer in Figs. 2 and 4 (a), and an underlying compact layer between the precipitate and the steel. Evidence for such a nonporous corrosion product was obtained by nanoindentation measurements, which revealed submicron-thick regions close to the metal with elastic modulus approaching that of compact iron oxide [21, 22].

Figure 6 shows an EDS line scan across a corroded grain boundary in a sample exposed for 2 hr at -0.521 V. The major species in the corrosion product layer are iron, oxygen and carbon, consistent with a product layer composed of iron hydroxy-carbonates [15]. The composition is close to that of the top surface corrosion product but without significant levels of sodium deriving from $NaHCO_3$ electrolyte. According to Blengino et al., product layers exhibit variable quantities of incorporated electrolyte ions depending on the corrosion rate [15]. Manganese, the primary alloying element in X70 steel, is apparently selectively excluded from the product layer, while silicon from the alloy is selectively oxidized and incorporated into the product. Silicon can significantly affect IGC in austenitic stainless steels, but we know of no prior reports of silicon effects on IGC or SCC of pipeline steels, or evidence for selective oxidation of Si at grain boundaries in X70 [16, 27]. Prior analytical TEM measurements of X52 and X65 steels revealed grain boundary segregation of only Mn solute, and atom probe tomography showed evidence for C segregation in X52 and X70 steels [28-30].

Additional small-angle cross sections were prepared on a sample exposed at -0.521 V for 15 min. At these early times, the cross sections revealed scattered corrosion product particles and isolated evidence of grain boundary attack at triple junctions, consistent with previous observations [13, 15]. Therefore, the current rise during polarization at constant potential (Fig. 1 (b)) correlates with spreading of intergranular attack to an increasing fraction of the surface grain boundaries. This interpretation was suggested previously by Riley and Sykes [13]. Similar current transients with maxima were recently found during CO_2 corrosion of carbon steel near pH 6, and the current rise was interpreted differently in terms of voids caused by crystallite nucleation in an amorphous surface film, or pH decrease due to carbonate precipitation [31, 32].

Fig. 7 exhibits small-angle cross sections of steel exposed at -0.478 V for 1 hr, for which the current density transient is given in Fig. 1 (b). Fig. 7 (a) shows the entire thickness of the IGC layer, while Fig. 7 (b) represents the interface between steel and the top product layer, and Fig. 7 (c) shows the midsection of the corroded region. As at -0.521 V, corrosion at -0.478 V is localized at triple junctions, and extends into lateral grain boundaries surrounding the triple junctions. Comparison of the interface images Fig. 7 (b) and Fig. 4 (c) reveals that, despite the smaller exposure time at -0.478 V, there is a significantly larger number density of corroded grain boundary triple junctions at the higher potential, and consequently greater penetration of corrosion product between grains. Apparently, the rate of spreading of IGC among grain boundaries increases with potential, correlating with the faster increase of current density with time after the initial minimum (Fig. 1 (b)).

Fig. 8 shows small-angle cross sections for a 50 min corrosion experiment at a potential of -0.575 V, close to the active dissolution peak of the steel polarization curve. The susceptibility of steel to SCC is considered to be lower at such potentials in comparison to potentials closer to

the passivation potential [4]. The images in Fig. 8 represent an area near a deposit of corrosion product, which in this experiment covered only a small portion of the surface. Fig. 8 (a) shows the entire thickness of the IGC layer, Fig. 8 (b) the steel-product layer interface, and Fig. 8 (c) shows the midsection of the corroded region. In contrast to the two more positive potentials, the cross-sectional images at -0.575 V revealed almost no detectable internal corrosion product at grain boundaries. Instead, IGC is characterized by selective dissolution of grains.

3.5. Transient electrochemical and stress measurements.

In this section, in situ stress measurements during intergranular corrosion are presented and discussed in view of the observations of IGC morphology evolution. Fig. 9 (a) displays current density and force per width transients from experiments at each of the three test potentials, and the charge density obtained by integration of the current is shown in Fig. 9 (b). Force per width at -0.478 V and -0.521 V increased steadily in the compressive direction during polarization. After an initial compressive period at -0.575 V, the force changed direction at 9 min, and exhibited a net tensile change at 60 min. From the trends in Fig. 9, it is clear that compressive stress generation correlates with internal corrosion product formation: extensive grain boundary corrosion product was found at the two higher potentials, but none at -0.575 V.

Stress is produced during oxide layer formation by strain associated with the volume increase upon conversion of metal to oxide [33]. The same principle can be applied to the present hydroxide-carbonate layers. As a first approximation, stress is modeled in a flat nonporous corrosion product film of uniform thickness, which comprises an inner dense layer between the metal and an outer stress-free porous precipitated corrosion product (Fig. 5). As mentioned

above, the presence of this compact layer was revealed by nanoindentation measurements [21, 22]. Since adherence of the surface film with the metal requires compatibility of the net in-plane strain at the metal-film interface, the formation of the compact layer must result in elastic or plastic strain within the film. It is assumed that the oxidation-induced strain-thickness product of the film is isotropic and hence given by $\Delta V_{m/f}/3$, where $\Delta V_{m/f}$ is the net volume expansion per unit area at the metal-film interface during metal oxidation [33],

$$\Delta V_{m/f} = \frac{q\Omega_p}{2F}\left(t_A - \frac{1}{\Phi}\right) \tag{4}$$

Here q is the anodic charge density, F is Faraday's constant, Ω_p is the molar volume of corrosion product, Φ is the Pilling-Bedworth ratio (the ratio of corrosion product to metal volume), and t_A is the average transport number for inward electrical migration of OH^- and CO_3^{-2} anions in the product layer. The anion transport number represents the fraction of current associated with film growth at the metal interface, with the remaining fraction (1 - t_A) due to outward metal ion migration resulting in growth of the precipitated film. In Eq. (4), t_A is the thickness of corrosion product formed at the metal interface per overall layer thickness, and $1/\Phi$ is the consumed metal thickness per product layer thickness.

Assuming hypothetically that the strain in the product layer is elastic in nature, the force per width would be given by

$$F_w = -\frac{Y_s \Delta V_{m/f}}{3(1-\nu_s)} \tag{5}$$

Combining Eqs. (3) and (4), the elastic stress generated is

$$F_w = \frac{\Omega_p Y_s q}{6F(1-\nu_s)}\left(\frac{1}{\Phi} - t_A\right) \quad (6)$$

While t_A in the product layer is unknown, passive films on iron and steel generally support both cation and anion transport by migration through grain boundaries between nanocrystals [34], and the presence of the outer precipitated product layer indicates that t_A must be less than unity. For an example calculation, t_A is taken to be 0.5, with Ω_p and Φ assigned values of 26.4 cm^3/mol and 3.7 for $Fe(OH)_2$. For the maximum charge density of 300 mC/cm^2 in Fig. 9 (b), the calculated force is close to -10^4 N/m, two orders of magnitude higher than the measured value. Therefore, despite the uncertain transport number, it is likely that the volume expansion due to oxide formation is accommodated by plastic rather than elastic deformation. The yield stress of the compact corrosion product was estimated to be 330 MPa from nanoindentation hardness measurements [22]. At the force levels in Fig. 9 (a), the compact product layer thickness would be F_w/σ_Y or 100 to 200 nm where σ_Y is the yield stress. This range is compatible with the submicron layer thickness of the compact layer revealed by nanoindentation [22]. Thus, the calculation supports the view that the porous precipitated layer is stress-free.

If the stress in the product layer remains close to the yield stress, the force can be approximated as $F_w \cong \sigma_Y h_p (A_p/A_s)$. Here σ_Y and h_p are the yield stress and thickness of the compact portion of the product layer, A_p is the area covered by the product layer (i. e. the entire oxidized surface area along grain boundaries) and A_s is the projected steel surface area. Assuming that the compact layer thickness remains constant, the increase of compressive force over time is due to increase of A_p as intergranular corrosion spreads over the surface and penetrates into the metal. Thus, the stress measurement is seen to be a sensitive indicator of

internal oxidation during intergranular corrosion, arising specifically from the compact product layer and not from the precipitated porous oxide seen in SEM. Indeed, the force transient at -0.575 V suggests oxidation at times less than 10 min, which is not apparent in cross-sectional SEM images at later times. Note that Fig. 9 (a) reveals different time dependence of force and current density at the two higher potentials: while force increases steadily, current density reaches a maximum and then decays. The different trends arise because current density depends on both corroding area and the corrosion product thickness, increasing at first as IGC spreads and decreasing at longer times due to growth of the outer product film.

3.6. Relevance to mechanisms of intergranular corrosion and stress corrosion cracking.

The present morphological observations reveal that at potentials of -0.521 and -0.478 V in the range of high SCC susceptibility, intergranular corrosion is centered at triple junctions and penetrates into lateral grain boundaries surrounding the triple junction. High-angle cross section images at -0.521 V show that corrosion at triple junctions takes the form of triangular wedges or notches, as illustrated in Fig. 5. At a potential near the active dissolution peak, the images reveal no precipitated internal dissolution product, and corrosion proceeds by selective grain etching. The shallow wedge shape near the passivation potential is explained by a constant dissolution velocity V_s on the grain surface and a slightly higher velocity V_{gb} at the grain boundary itself (Eq. (3)). Stress measurements provide evidence for a compact surface layer at the two higher potentials, which likely regulates V_s. The mechanism explaining the higher dissolution rate on the boundary is less evident. Open crevices are found along corroding grain boundaries at -0.521 V and -0.478 V (Fig. 5), and the absence of a porous product would reduce the resistance for mass

transport along the boundary. Others have proposed that grain boundary segregated carbon is important for intergranular SCC of low-carbon steels [30, 35]. However, SEM images of shallow angle-polished specimens reveal no evidence for segregated phases at the boundaries. Wedging stresses due to the compact corrosion product layer at the grain boundary could assist corrosion propagation along the boundary [17].

The IGC morphology evolution described here may be related to the strong correspondence between the potential and pH ranges for SCC and IGC [7, 36]. Wendler-Kalsch suggested that wedges produced by corrosion at grain boundaries may induce sufficient stress concentrations to initiate stress corrosion cracks [5]. Indeed, a critical finding of both Ref. [5] and the present work is that wedge or notch features are found only in the potential range where steel is vulnerable to SCC. However, it is not clear that the relatively blunt wedges in Fig. 2 can generate significant stress concentration to influence SCC. It is possible that notches with smaller angles and hence larger stress concentrations may be produced at longer exposure times, or by synergistic enhancement of intergranular corrosion by external stress [7]. Another possible reason for the importance of grain boundary oxidation in SCC is suggested by the EDS measurements in Fig. 6 which revealed selective oxidation of Si solute atoms. Preferential oxidation of reactive solutes may produce non-equilibrium metal vacancies, and vacancy-dislocation interaction can explain the reduced local hardness near corroded grain boundaries recently detected by nanoindentation [22, 37]. Since vacancies associated with grain boundary oxidation would be present only at potentials or high cracking susceptibility, the possible involvement of vacancies in the SCC mechanism should be considered. A third possible role of grain boundary oxidation in SCC is that wedging stresses due to the compact corrosion product layer at the grain boundary could directly assist grain boundary fracture [17].

4. Conclusions

The present article reports characterization of morphology and stress evolution during intergranular corrosion of X70 pipeline steel to aqueous 1 M $NaHCO_3$ solution at pH 8.1. At active dissolution potentials close to the passivation potential, for which the steel is susceptible to intergranular stress-corrosion cracking, IGC produces triangular wedges of porous corrosion product centered around grain boundary triple junctions. The wedge shape is due to a higher corrosion rate at the grain boundary itself compared to that on the grain surfaces. Corrosion penetrates along triple junctions while it also spreads laterally into adjacent grain boundaries. Closer to the potential of the active current peak, intergranular corrosion proceeds by selective dissolution of grains with no evidence of internal oxidation. In situ stress measurements close to the passivation potential revealed compressive stress generation due to formation of a compact corrosion product layer along corroding grain surfaces, but a net tensile stress change at a potential close to the current peak at which no internal oxidation was found. Si solute atoms are selectively oxidized into the grain boundary corrosion product. Overall, the results demonstrate that grain boundary oxidation associated with corrosion product wedges occurs at potentials for which X70 steel is vulnerable to SCC.

Acknowledgments

The authors are thankful the support from U.S. Department of Transportation, Pipeline and Hazardous Materials Safety Administration under Competitive Academic Agreement Program No. DTPH5614HCAP03 and DTPH5614HCAP01.

References

[1] Y.F. Cheng, Stress Corrosion Cracking of Pipelines, Wiley, 2013.

[2] F.F. Eliyan, A. Alfantazi, Mechanisms of Corrosion and Electrochemical Significance of Metallurgy and Environment with Corrosion of Iron and Steel in Bicarbonate and Carbonate Solutions - A Review, Corrosion, 70 (2014) 880-898.

[3] J.M. Sutcliffe, W.K. Boyd, R.R. Fessler, R.N. Parkins, Stress Corrosion Cracking of Carbon Steel in Carbonate Solutions, Corrosion, 28 (1972) 313-320.

[4] R.D. Armstrong, A.C. Coates, Correlation between Electrochemical Parameters and Stress Corrosion Cracking, Corros. Sci., 16 (1976) 423-433.

[5] E. Wendler-Kalsch, The effects of film formation and mechanical factors on the initiation of stress corrosion cracking of unalloyed steels in carbonate solutions, Werkst. Korros., 31 (1980) 531-542.

[6] R.N. Parkins, S. Zhou, The stress corrosion cracking of C-Mn steel in CO_2-HCO_3^--CO_3^{2-} solutions. I. Stress corrosion data, Corros. Sci., 39 (1997) 159-173.

[7] R.N. Parkins, S. Zhou, The stress corrosion cracking of C-Mn Steel in CO_2-HCO_3^--CO_3^{2-} solutions. II. Electrochemical and other data, Corros. Sci., 39 (1997) 175-191.

[8] R.C. Newman, Stress-Corrosion Cracking Mechanisms, in: P. Marcus (Ed.) Corrosion Mechanisms in Theory and Practice, CRC Press, Boca Raton, 2011, pp. 499-544.

[9] R.D. Armstrong, A.C. Coates, Passivation of Iron in Carbonate-Bicarbonate Solutions, J. Electroanal. Chem., 50 (1974) 303-313.

[10] D.H. Davies, G.T. Burstein, The Effects of Bicarbonate on the Corrosion and Passivation of Iron, Corrosion, 36 (1980) 416-422.

[11] C.R. Valentini, C.A. Moina, J.R. Vilche, A.J. Arvia, The Electrochemical Behavior of Iron in Stagnant and Stirred Potassium Carbonate-Bicarbonate Solutions in the 0-75^{o}C Temperature Range, Corros. Sci., 25 (1985) 985-997.

[12] E.B. Castro, C.R. Valentini, C.A. Moina, J.R. Vilche, A.J. Arvia, The Influence of Ionic Composition on the Electrodissolution and Passivation of Iron Electrodes in Potassium Carbonate Bicarbonate Solutions in the 8.4-10.5 pH Range at 25^{o}C, Corros. Sci., 26 (1986) 781-793.

[13] A.M. Riley, J.M. Sykes, The Active Passive Transition in Low-Alloy Steels in Carbonate Solutions, Electrochim. Acta, 35 (1990) 35-45.

[14] E.B. Castro, J.R. Vilche, A.J. Arvia, Iron Dissolution and Passivation in K_2CO_3-$KHCO_3$ Solutions - Rotating-Ring-Disk Electrode and XPS Studies, Corros. Sci., 32 (1991) 37-50.

[15] J.M. Blengino, M. Keddam, J.P. Labbe, L. Robbiola, Physicochemical Characterization of Corrosion Layers Formed on Iron in a Sodium Carbonate-Bicarbonate Containing Environment, Corros. Sci., 37 (1995) 621-643.

[16] B. Gwinner, M. Auroy, F. Balbaud-Celerier, P. Fauvet, N. Larabi-Gruet, P. Laghoutaris, R. Robin, Towards a reliable determination of the intergranular corrosion rate of austenitic stainless steel in oxidizing media, Corros. Sci., 107 (2016) 60-75.

[17] D. McNaughtan, M. Worsfold, M.J. Robinson, Corrosion product force measurements in the study of exfoliation and stress corrosion cracking in high strength aluminium alloys, Corros. Sci., 45 (2003) 2377-2389.

[18] T. Zhang, W.Y. Chu, K.W. Gao, L.J. Qiao, Study of correlation between hydrogen-induced stress and hydrogen embrittlement, Mater. Sci. Eng., A, 347 (2003) 291-299.

[19] H.E. Evans, H.Y. Li, P. Bowen, A mechanism for stress-aided grain boundary oxidation ahead of cracks, Scripta Mater., 69 (2013) 179-182.

[20] Ö.Ö. Çapraz, S. Ide, P. Shrotriya, K.R. Hebert, Tensile stress and plastic deformation in aluminum induced by aqueous corrosion, Acta Mater., 115 (2016) 434-441.

[21] D. Yavas, P. Mishra, A.F. Bastawros, K.R. Hebert, P. Shrotriya, Characterization of Sub-surface Damage During the Early Stage of Stress Corrosion Cracking by Nano Indentation, C Proc Soc Exp Mech, (2017) 37-44.

[22] D. Yavas, P. Mishra, A. Alshehri, P. Shrotriya, K.R. Hebert, A.F. Bastawros, Nanoindentation study of corrosion-induced grain boundary degradation in a pipeline steel, Electrochem. Commun., 88 (2018) 88-92.

[23] J. Wang, P. Shrotriya, K.S. Kim, Surface residual stress measurement using curvature interferometry, Exp. Mech., 46 (2006) 39-46.

[24] Ö.Ö. Çapraz, K.R. Hebert, P. Shrotriya, In Situ Stress Measurement During Aluminum Anodizing Using Phase-Shifting Curvature Interferometry, J. Electrochem. Soc., 160 (2013) D501-D506.

[25] G.E. Fougere, L. Riester, M. Ferber, J.R. Weertman, R.W. Siegel, Young's modulus of nanocrystalline Fe measured by nanoindentation, Mater. Sci. Eng., A, 204 (1995) 1-6.

[26] L. Beaunier, M. Froment, C. Vignaud, A Kinetical Model for the Electrochemical Grooving of Grain Boundaries, Electrochim. Acta, 25 (1980) 1239-1246.

[27] O.V. Kasparova, Peculiarities of intergranular corrosion of silicon-containing austenitic stainless steels, Prot. Met, 40 (2004) 425-431.

[28] J.Q. Wang, A. Atrens, D.R. Cousens, P.M. Kelly, C. Nockolds, S. Bulcock, Measurement of grain boundary composition for X52 pipeline steel, Acta Mater., 46 (1998) 5677-5687.

[29] J.Q. Wang, A. Atrens, D.R. Cousens, C. Nockolds, S. Bulcock, Boundary characterisation of X65 pipeline steel using analytical electron microscopy, Journal of Materials Science, 34 (1999) 1711-1719.

[30] A. Atrens, J.Q. Wang, K. Stiller, H.O. Andren, Atom probe field ion microscope measurements of carbon segregation at an α:α grain boundary and service failures by intergranular stress corrosion cracking, Corros. Sci., 48 (2006) 79-92.

[31] B. Ingham, M. Ko, N. Laycock, J. Burnell, P. Kappen, J.A. Kimpton, D.E. Williams, In situ synchrotron X-ray diffraction study of scale formation during CO_2 corrosion of carbon steel in sodium and magnesium chloride solutions, Corros. Sci., 56 (2012) 96-104.

[32] B. Ingham, M. Ko, N. Laycock, N.M. Kirby, D.E. Williams, First stages of siderite crystallisation during CO_2 corrosion of steel evaluated using in situ synchrotron small- and wide-angle X-ray scattering, Faraday Discuss., 180 (2015) 171-190.

[33] J.C. Nelson, R.A. Oriani, Stress Generation During Anodic-Oxidation of Titanium and Aluminum, Corros. Sci., 34 (1993) 307-326.

[34] P. Marcus, V. Maurice, H.H. Strehblow, Localized corrosion (pitting): A model of passivity breakdown including the role of the oxide layer nanostructure, Corros. Sci., 50 (2008) 2698-2704.

[35] L.M. Long, H.H. Uhlig, Effect of Carbon and Oxygen in Iron on Stress Corrosion Cracking in Nitrate Solution, J. Electrochem. Soc., 112 (1965) 964-967.

[36] R.N. Parkins, Mechanistic aspects of intergranular stress corrosion cracking of ferritic steels, Corrosion, 52 (1996) 363-374.

[37] E.K. Njeim, D.F. Bahr, Atomistic simulations of nanoindentation in the presence of vacancies, Scripta Mater., 62 (2010) 598-601.

List of Figures.

Figure 1. Electrochemical measurements during corrosion of X70 steel in 1 M $NaHCO_3$. (a) Linear sweep voltammetry showing the three test potentials used in other experiments. (b) Current density transients for the experiments used for morphology observations in Figs. 4-7.

Figure 2. Large-angle cross section views after corrosion at -0.521 V. Dashed lines indicate triangular wedge features produced by corrosion at the alloy-corrosion product interface. The angles of the wedge apex are marked in the image. (a) 2 hr exposure; sample prepared by FIB etching, cross section plane 52^o from horizontal. A 1 μm thick protective carbon layer covers the corrosion product. (b) 4 hr exposure; sample prepared by polishing, cross section plan 90^o from horizontal.

Figure 3. Height profile measured by optical profilometry after 2 hr exposure at -0.521 V and followed by removal of corrosion product. Curve to the left of the arrow represents an area that was not exposed to solution.

Figure 4. Small-angle cross section views of X70 steel after 2 hr corrosion at -0.521 V. Sample was prepared by shallow-angle polishing. Panels (b) - (e) are high-magnification images at the points indicated in the low-magnification image (a).

Figure 5. Schematic depiction of triangular wedge morphology of intergranular corrosion.

Figure 6. Composition of grain boundary corrosion product film on sample exposed for 2 hr at -0.521 V. (a) SEM showing location of EDS line scan. (b) Composition profile along the line scan.

Figure 7. Small-angle cross section views of X70 steel after 1 hr corrosion at -0.478 V. Sample was prepared by shallow-angle polishing. Panels (b) and (c) are high-magnification images at the points indicated in the low-magnification image (a).

Figure 8. Small-angle cross section views of X70 steel after 50 min corrosion at -0.575 V. Sample was prepared by shallow-angle polishing. Panels (b) and (c) are high-magnification images at the points indicated in the low-magnification image (a).

Figure 9. Stress and current density measurements during corrosion exposures at the three test potentials. (a) Force per width (solid lines) and current density (dashed lines) transients. (b) Charge density transients obtained by integrating the current density in (a).

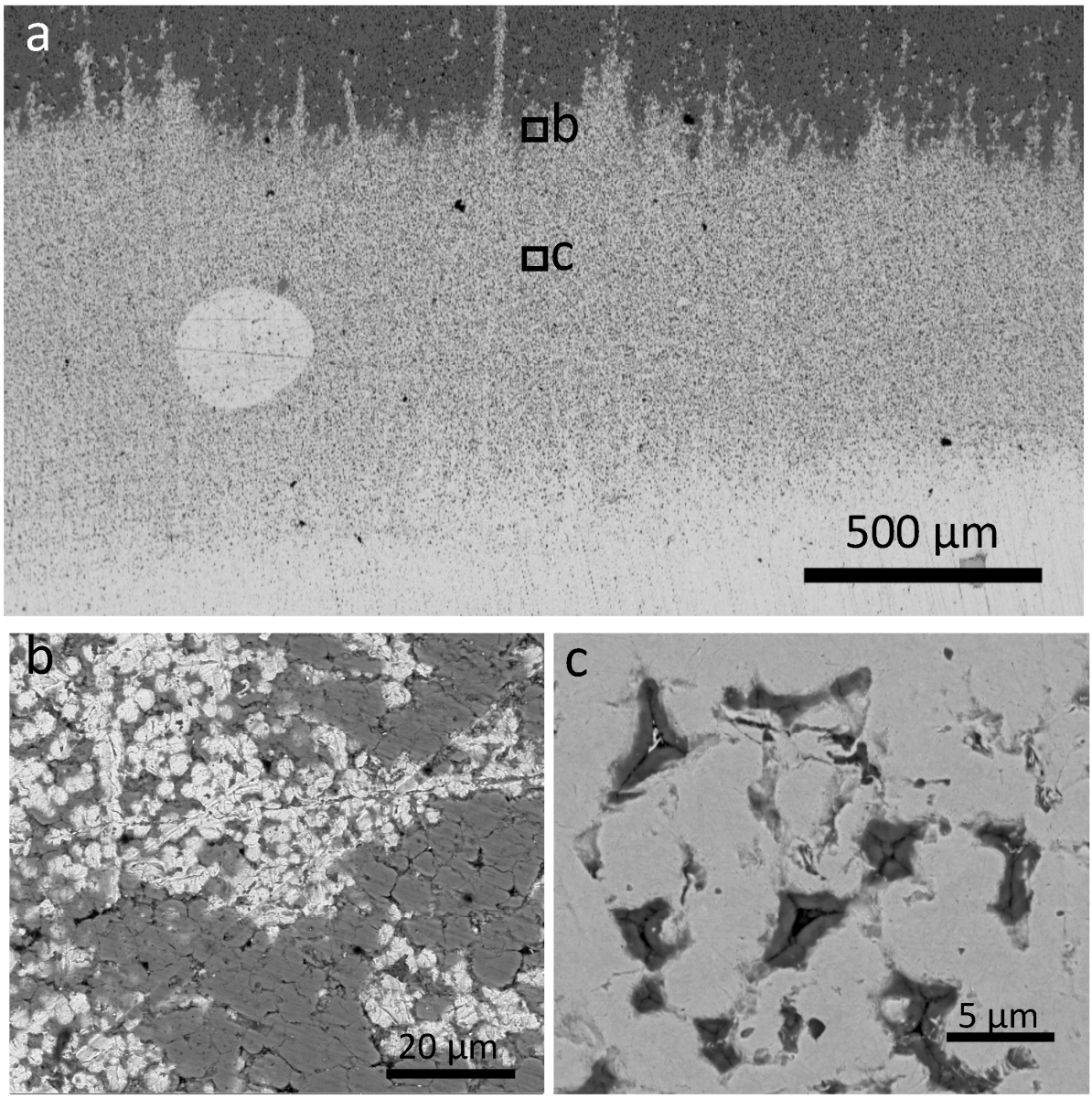

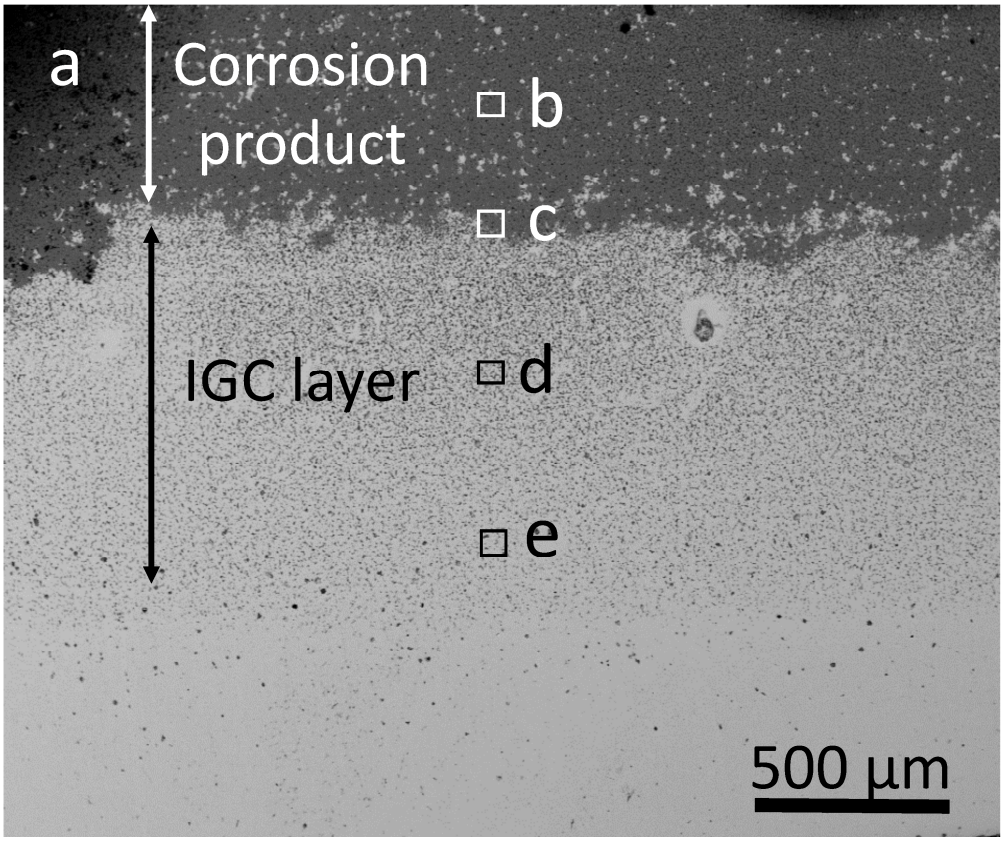
a
Corrosion product
b
c
IGC layer
d
e
500 µm

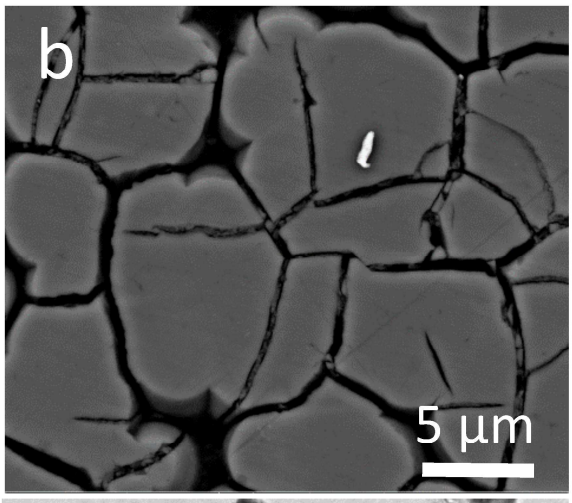
b
5 µm

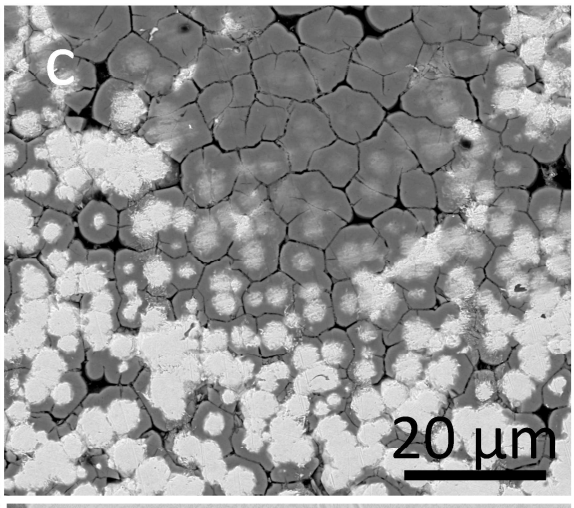
c
20 µm

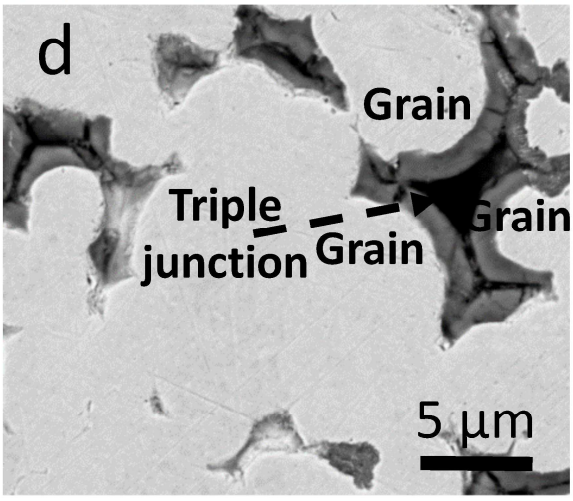
d
Grain
Triple junction
Grain
Grain
5 µm

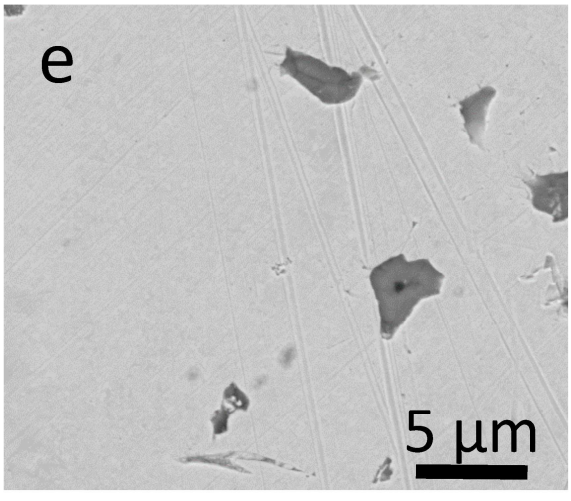
e
5 µm

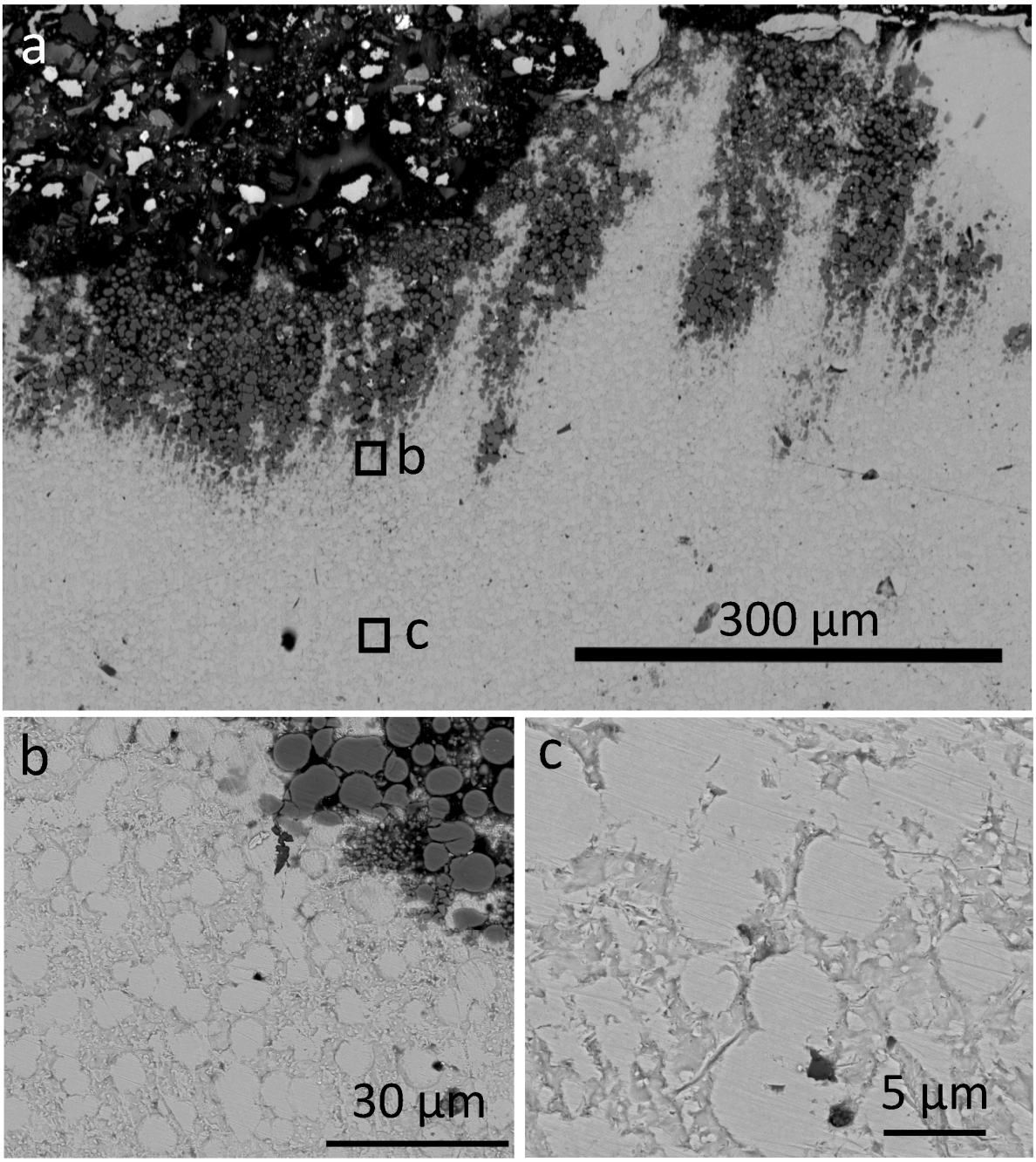
a
b
c
300 µm
b
30 µm
c
5 µm

a

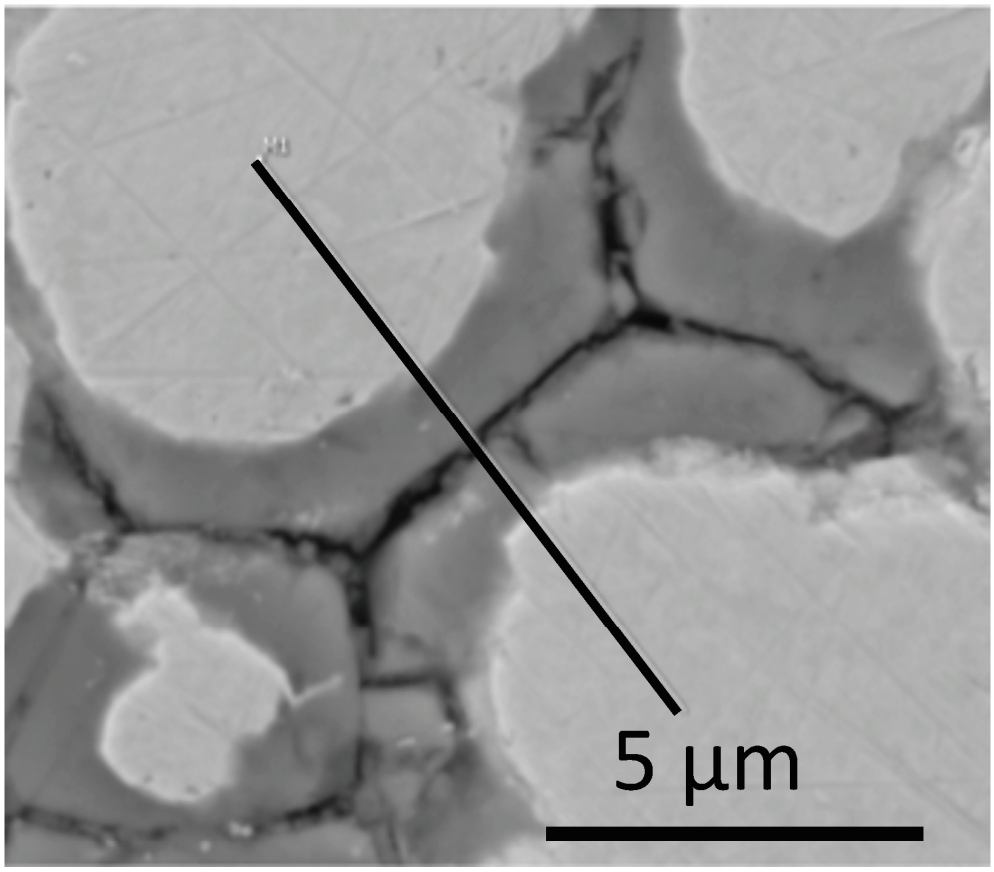
5 µm

b

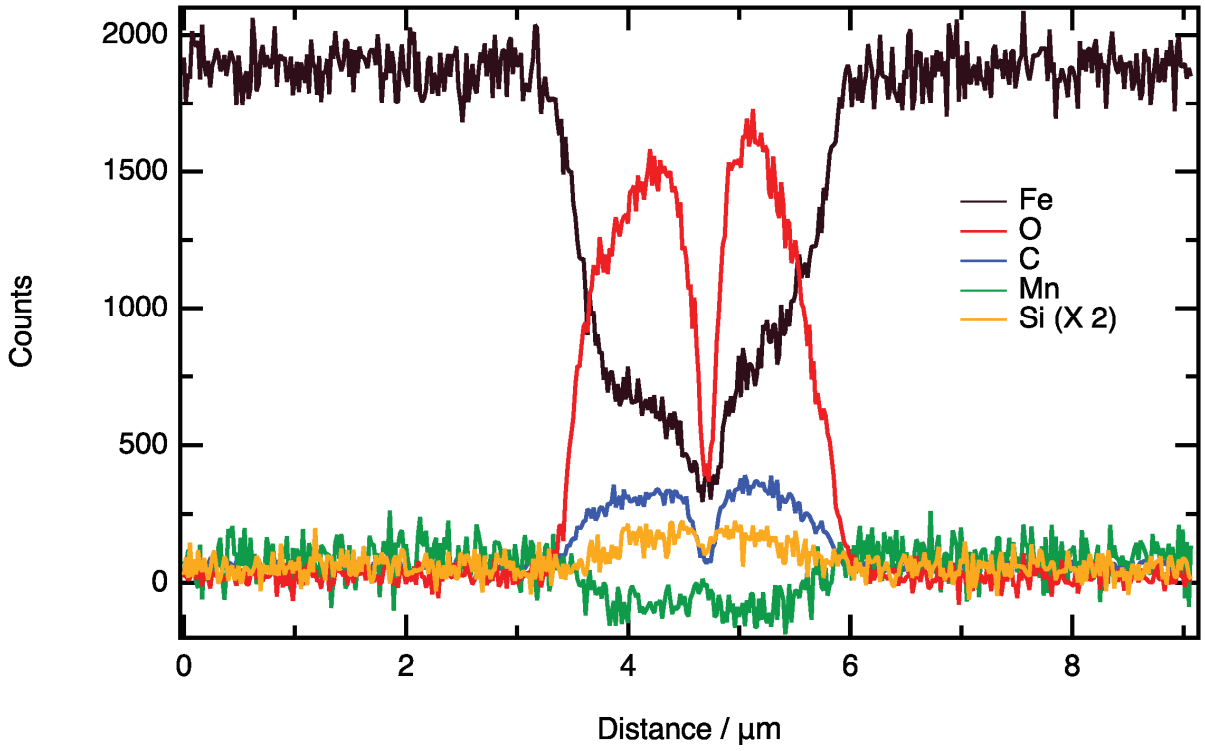
2000
1500
1000
500
0
Counts
0
2
4
6
8
Distance / µm
Fe
O
C
Mn
Si (X 2)

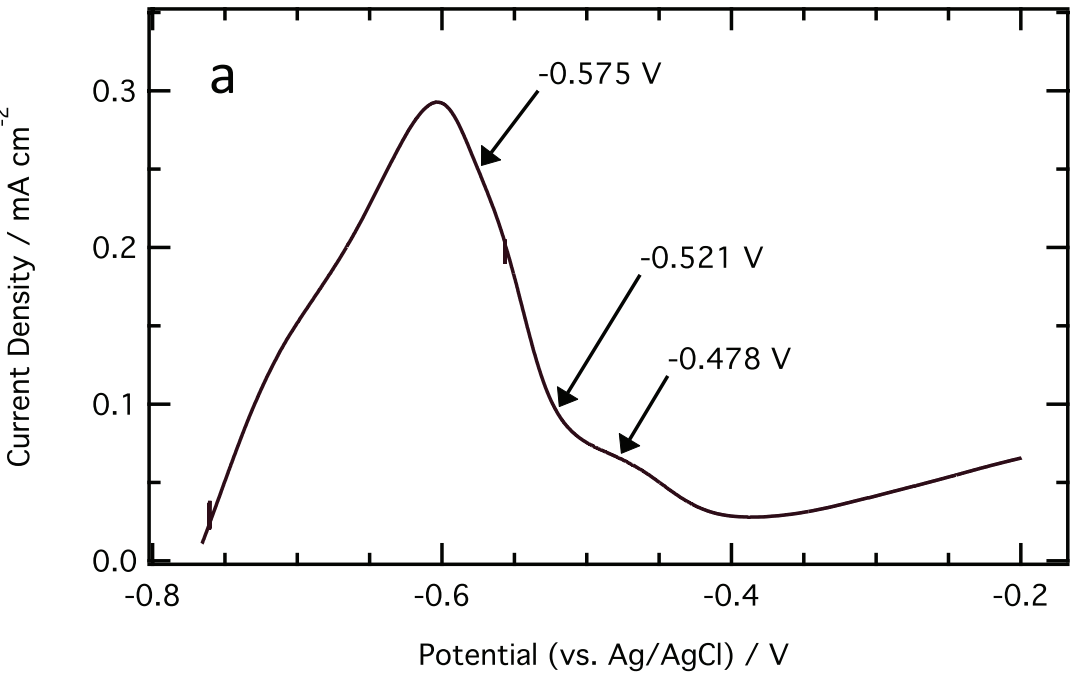

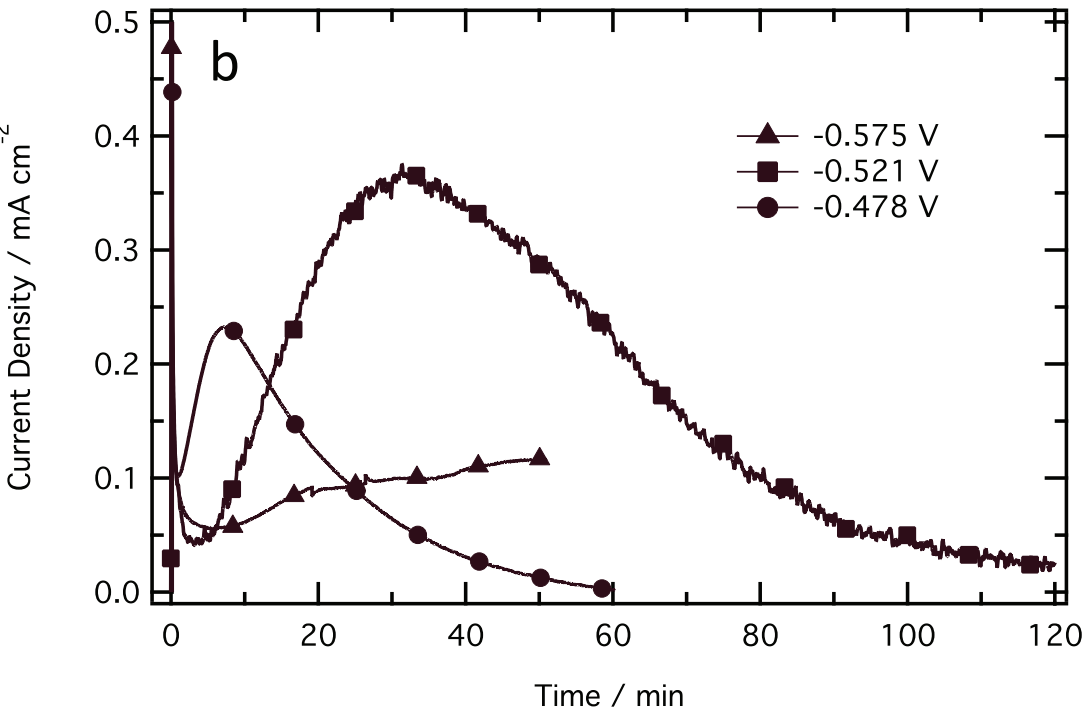

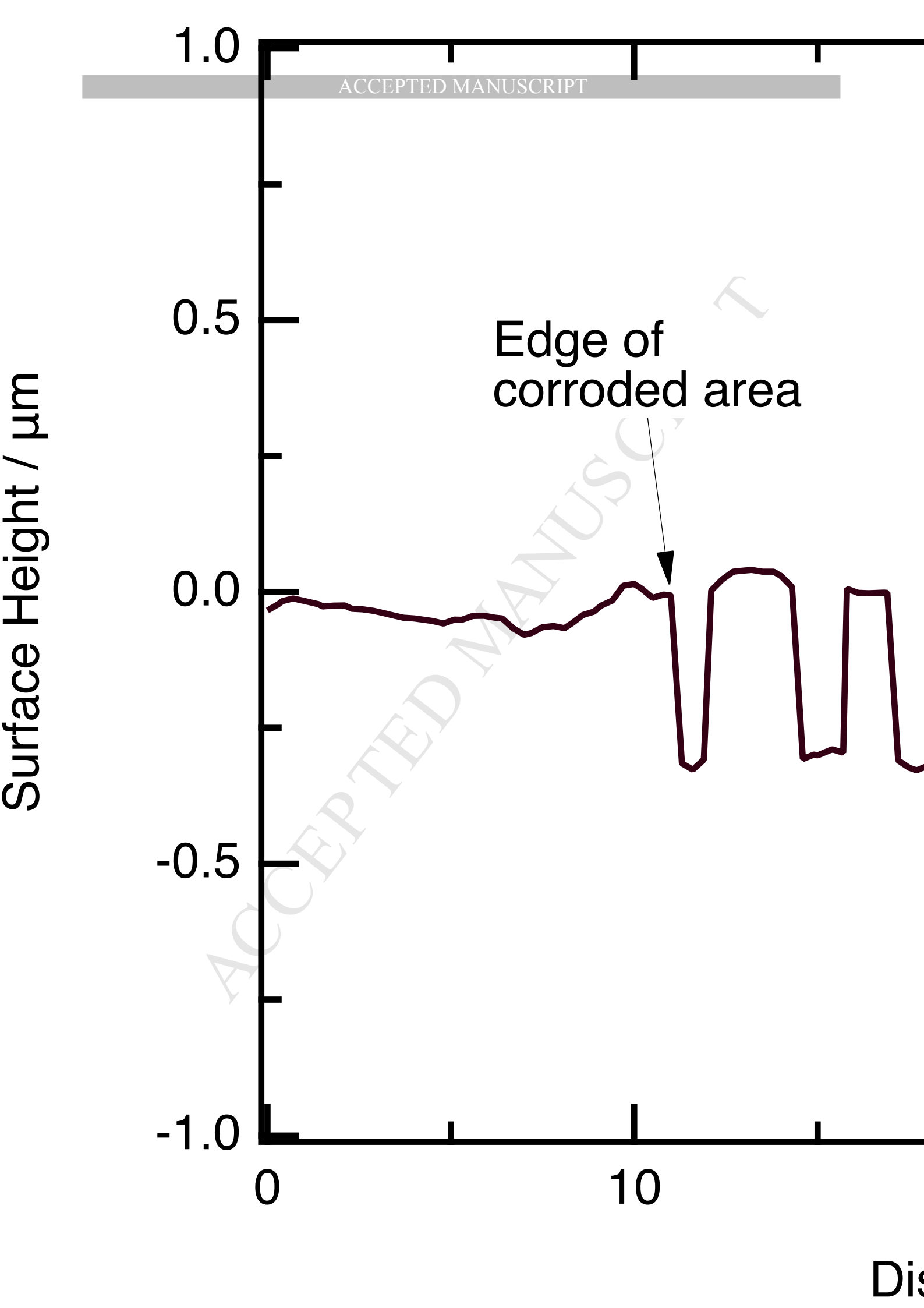

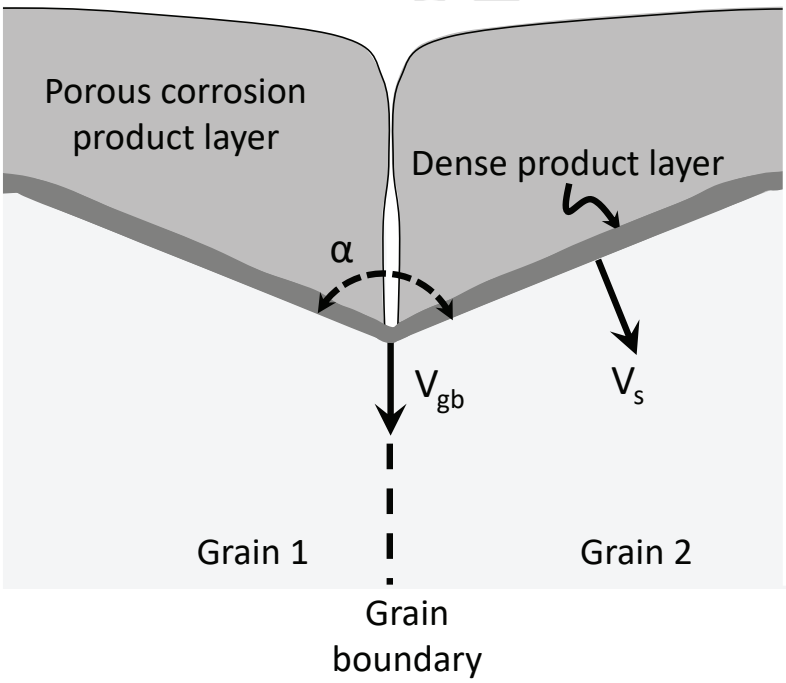

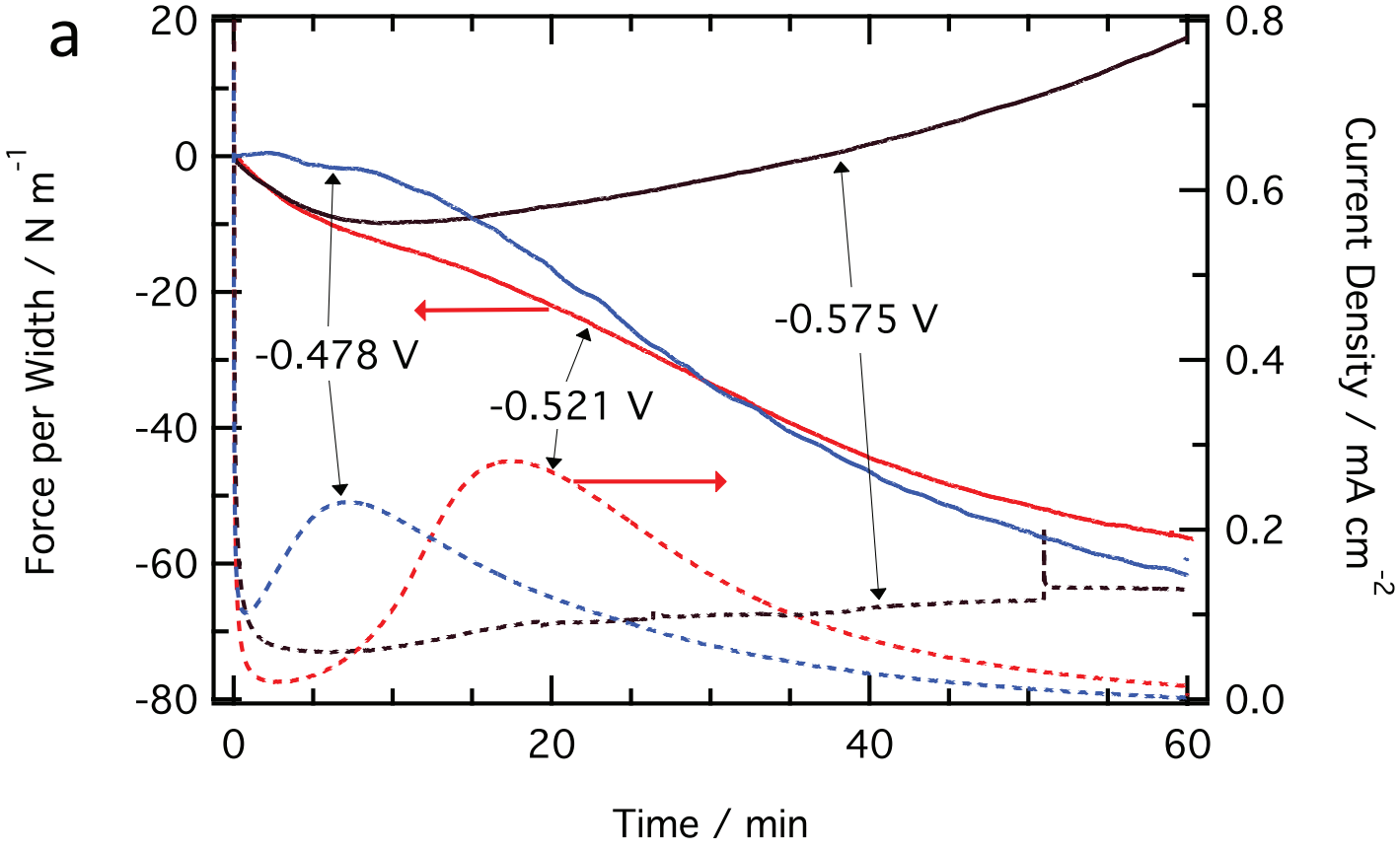
a
Force per Width / N m-1
Current Density / mA cm-2
Time / min
-0.478 V
-0.521 V
-0.575 V
20
0
-20
-40
-60
-80
0.8
0.6
0.4
0.2
0.0
0
20
40
60

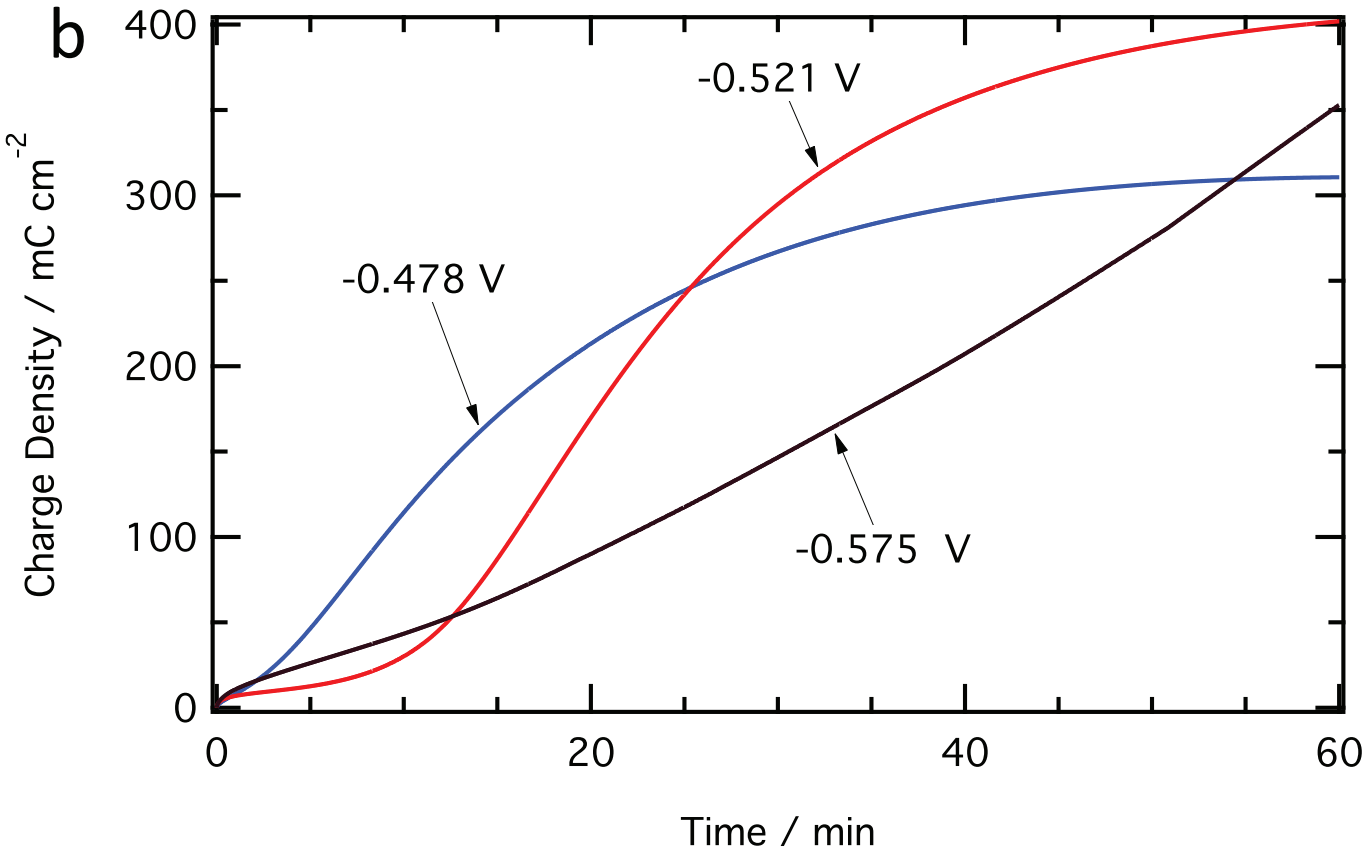
b
Charge Density / mC cm-2
Time / min
-0.521 V
-0.478 V
-0.575 V
400
300
200
100
0
0
20
40
60

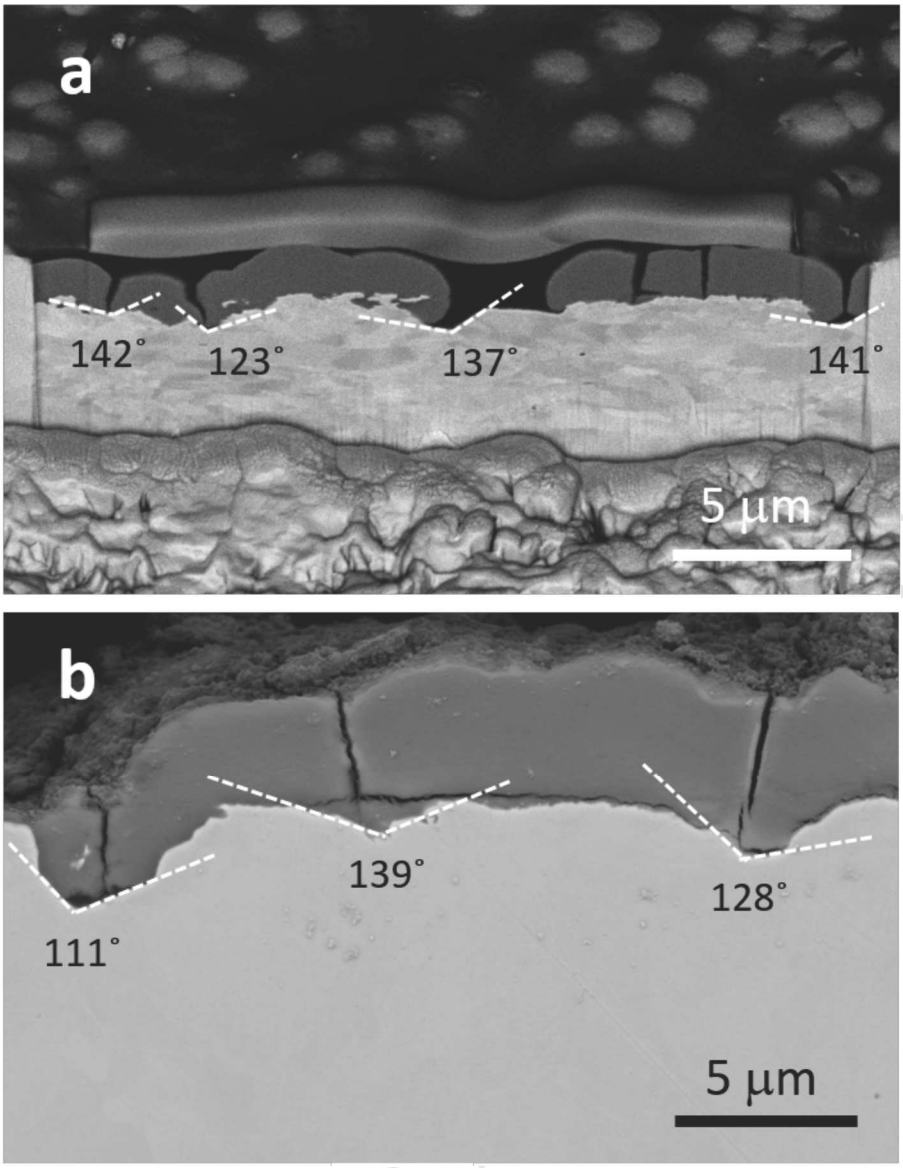

Highlights for "Morphology and Stress Evolution During the Initial Stages of Intergranular Corrosion of X70 Steel," D. Yavas[a], A. Alshehri[b], P. Mishra[c], P. Shrotriya[b], A. F. Bastawros[a], and K. R. Hebert

- Anodic polarization in bicarbonate solution leads to intergranular corrosion
- Wedges of oxide-carbonate product form at grain boundary triple junctions
- Internal oxidation on grain boundaries generates compressive stress
- Grain boundaries oxidize only at potentials of stress corrosion susceptibility
- Silicon in steel is selectively oxidized into grain boundary corrosion product